THE JOURNAL OF CHEMICAL PHYSICS **146**, 052820 (2017)

Low temperature thermal ALD of a SiN_x interfacial diffusion barrier and interface passivation layer on $Si_xGe_{1-x}(001)$ and $Si_xGe_{1-x}(110)$

Mary Edmonds,[1] Kasra Sardashti,[1] Steven Wolf,[1] Evgueni Chagarov,[2] Max Clemons,[3] Tyler Kent,[1] Jun Hong Park,[1] Kechao Tang,[4] Paul C. McIntyre,[4] Naomi Yoshida,[5] Lin Dong,[5] Russell Holmes,[6] Daniel Alvarez,[6] and Andrew C. Kummel[1,2,a)]
[1]*Materials Science and Engineering Program, University of California, San Diego, La Jolla, California 92093, USA*
[2]*Department of Chemistry and Biochemistry, University of California, San Diego, La Jolla, California 92093, USA*
[3]*Department of Electrical and Computer Engineering, University of California, San Diego, La Jolla, California 92093, USA*
[4]*Department of Materials Science and Engineering, Stanford University, Stanford, California 94305, USA*
[5]*Applied Materials, Sunnyvale, California 94085, USA*
[6]*Rasirc, Inc., San Diego, California 92126, USA*

(Received 5 September 2016; accepted 21 December 2016; published online 2 February 2017)

Atomic layer deposition of a silicon rich SiN_x layer on $Si_{0.7}Ge_{0.3}(001)$, $Si_{0.5}Ge_{0.5}(001)$, and $Si_{0.5}Ge_{0.5}(110)$ surfaces has been achieved by sequential pulsing of Si_2Cl_6 and N_2H_4 precursors at a substrate temperature of 285 °C. XPS spectra show a higher binding energy shoulder peak on Si 2p indicative of $SiO_xN_yCl_z$ bonding while Ge 2p and Ge 3d peaks show only a small amount of higher binding energy components consistent with only interfacial bonds, indicating the growth of SiO_xN_y on the SiGe surface with negligible subsurface reactions. Scanning tunneling spectroscopy measurements confirm that the SiN_x interfacial layer forms an electrically passive surface on p-type $Si_{0.70}Ge_{0.30}(001)$, $Si_{0.50}Ge_{0.50}(110)$, and $Si_{0.50}Ge_{0.50}(001)$ substrates as the surface Fermi level is unpinned and the electronic structure is free of states in the band gap. DFT calculations show that a Si rich a-$SiO_{0.4}N_{0.4}$ interlayer can produce lower interfacial defect density than stoichiometric a-$SiO_{0.8}N_{0.8}$, substoichiometric a-Si_3N_2, or stoichiometric a-Si_3N_4 interlayers by minimizing strain and bond breaking in the SiGe by the interlayer. Metal-oxide-semiconductor capacitors devices were fabricated on p-type $Si_{0.7}Ge_{0.3}(001)$ and $Si_{0.5}Ge_{0.5}(001)$ substrates with and without the insertion of an ALD SiO_xN_y interfacial layer, and the SiO_xN_y layer resulted in a decrease in interface state density near midgap with a comparable C_{max} value. *Published by AIP Publishing.* [http://dx.doi.org/10.1063/1.4975081]

I. INTRODUCTION

Si_xGe_{1-x} intrinsically has high hole mobility which can be further enhanced by compressively straining the crystal lattice by growing Si_xGe_{1-x} on a substrate with a lower Ge content.[1–3] As semiconductor device manufacturing continues the scaling of gate stacks to the subnanometer equivalent oxide thickness (EOT) regime, thin film deposition requires high conformality with nucleated growth in every unit cell to ensure low defect density and low gate leakage. Passivation and functionalization of the Si_xGe_{1-x} surface remains challenging as Ge surface dangling bonds act to pin the SiGe surface Fermi level, and Ge sub-oxide surface species degrade semiconductor mobility and create a higher density of interfacial trap states in the band gap.[4,5] Plasma nitridation of pure Ge[6–9] and low content Ge (x = 0.5-1) Si_xGe_{1-x}surfaces[10] has served as an effective passivating interfacial layer between the semiconductor and oxide by maintaining a low density of interfacial trap states; in addition, it prevents Ge out-diffusion into the oxide.[7,10] However, it remains challenging to fully nitridate surface Ge atoms present at the SiGe surface because silicon is more reactive than germanium leading to formation of a non-uniform interfacial layer.[10] However, plasma post-nitridation of $Al_2O_3/Si_{0.75}Ge_{0.25}$ gate stacks has been shown to decrease the density of interfacial trap states at the cost of increasing the EOT.[11]

Low temperature CVD growth of silicon nitride films on Si(001) substrates by dosing Si_2Cl_6 followed by N_2H_4 at 350 °C–400 °C substrate temperatures at a relatively high deposition pressure of 160 Torr has also been previously reported.[12] The reported CVD silicon nitride films contained ~30 at. % hydrogen, which may be due to the absence of purge steps between half cycle reactions or the high deposition pressure. Silicon nitride plasma assisted ALD has been previously reported on ZnSe substrates at 350 °C–450 °C by alternating pulses of Si_2Cl_6 and NH_3 plasma.[13] Si_2Cl_6 was pulsed for 30 s at a peak chamber pressure of 70 mTorr followed by a 30 s Ar purge at 80 mTorr. The NH_3 plasma was produced with an argon carrier gas at a total dose pressure of 100 mTorr. The report shows highly conformal SiN_x deposited films of ~30 nm thickness with a reported growth per cycle of ~1.2 Å.[13] Many similar plasma assisted silicon nitride ALD processes have been reported by employing alternating pulses

a)Author to whom correspondence should be addressed. Electronic mail: akummel@ucsd.edu

of NH_3 plasma and a silane precursor (SiH_4, SiH_2Cl_2, $SiCl_4$, and Si_3Cl_8) at temperature ranges of 350 °C–623 °C on silicon (001), germanium (001), and low Ge content SiGe (001) substrates.[14–19] Lower temperature plasma assisted ALD has also been reported through the sequential pulsing of NH_3 or N_2 plasma and a silane precursor (SiH_4, SiH_2Cl_2, and $N(SiH_3)_3$) at temperatures of 250 °C–500 °C on Si(001) substrates.[20–23] Room temperature silicon nitride deposition on Si(001) substrates has been reported by jet-vapor deposition of SiH_4 in a He carrier gas or an N_2 plasma in a He carrier gas.[24] The jet-vapor deposition process requires a specialized chamber set-up which may be difficult to scale to large area substrates with uniform coverage for subnanometer thickness on 3D structures (finFETs).

Thermal silicon nitride atomic layer deposition (ALD) has been previously reported by alternate pulses of Si_2Cl_6 (1 Torr pulses) and N_2H_4 (0.1 Torr pulses, 98% N_2H_4 and 2% H_2O) on an NH-terminated Si(001) surface.[25] The experiments employed both very high temperatures (>525 °C) and very long N_2H_4 half-cycle pulse time (12 min). The growth mechanism is in contrast to a report by Park *et al.* of thermal decomposition of Si_2Cl_6 at temperatures exceeding 500 °C.[26] For this high temperature Si_2Cl_6 and N_2H_4 reaction, Morishita *et al.* reported each precursor, Si_2Cl_6 and 98% N_2H_4 containing residual H_2O, was consecutively flowed into the reaction chamber (base pressure of 1×10^{-3} Torr) without carrier gas for a fixed time of 4 s; subsequently, all valves to precursor containers and pumping lines were shut so that the gas was left in the reaction chamber for the designated exposure time of 735 s. While the oxidant and reductant were dosed at separate times, this process may not be a true ALD process, as the stagnant Si_2Cl_6 gas in the reaction chamber may have a partial decomposition and introduce a CVD component; however, the pioneering work of Morishita *et al.* did show that low temperature N_2H_4 reactions might be feasible. The present study employs anhydrous hydrazine to help keep the Si–N_x surface free of unwanted oxygen or water contamination during film deposition; this was not part of the Morishita *et al.* process which produced 4% oxygen in film growth attributed to residual water in the hydrazine.[25]

In this work, subnanometer passivating (~6–10 Å) silicon nitride films have been deposited on low and high Ge content Si_xGe_{1-x}(001)/(110) surfaces by a plasma-free ALD process using Si_2Cl_6 and N_2H_4 at a low substrate temperature (285 °C) with low half-cycle pulse times and vacuum purges between precursor pulses. This study employs anhydrous hydrazine as the nitriding agent, both to keep the Si–N_x surface free of unwanted oxygen contamination and to eliminate plasma induced surface damage by nitriding the surface through a thermal ALD process. Metal-oxide-semiconductor capacitors (MOSCAP) device fabrication was performed on p-type $Si_{0.70}Ge_{0.30}$(001) and $Si_{0.5}Ge_{0.5}$(001) substrates with and without the insertion of a SiN_x passivating interfacial layer deposited by ALD and a decrease in extracted interface state density, particularly near midgap, was observed for a comparable C_{max} value for the SiN_x passivated surfaces compared to the non-passivated surface.

II. EXPERIMENTAL

This study employed p-type $Si_{0.7}Ge_{0.3}$(001) (Applied Materials, Inc.) and $Si_{0.5}Ge_{0.5}$(001) (GLOBALFOUNDRIES, Inc.) films epitaxially grown on p-type Si(001) substrates and p-type $Si_{0.5}Ge_{0.5}$(110) films epitaxially grown on p-type Si(110) substrates (GLOBALFOUNDRIES, Inc.). The Si_xGe_{1-x} surface underwent a degrease procedure by ultrasonication with acetone for 10 min, isopropyl alcohol for 10 min, and deionized water for 5 min. Next, the sample was dipped into a beaker containing a 2% HF/water solution with a layer of toluene on top for 2 min. After 2 min, the sample was pulled out through the layer of toluene and quickly transferred into the ultrahigh vacuum (UHV) preparation chamber with a base pressure of 1×10^{-10} Torr before the layer of toluene evaporated from the surface. This process was employed to prevent the sample from being air exposed following the 2% HF dip. The sample was subsequently characterized by an Omicron *in situ* monochromatic XPS, located inside the prep chamber, using the aluminum Kα excitation source ($h\nu = 1486.7$ eV) with spectra taken at a glancing angle of 30° to obtain enhanced surface sensitivity. XPS raw counts were collected using the XPS constant analyzer energy mode with a pass energy of 50 eV and line width of 0.1 eV. XPS peak shape analysis was conducted using CASA XPS v.2.3 by employing a Shirley background subtraction. All XPS raw core level peaks were corrected by Schofield photoionization cross sectional relative sensitivity factors. Following the initial sample XPS characterization, the sample was radiatively heated on the UHV manipulator (via a PBN heater) to 330 °C for 15 min in the UHV prep chamber; subsequently the sample was dosed with 1800 L of atomic hydrogen to remove surface carbon contamination; a Langmuir was defined at a flux of 10^{-6} Torr/s of gas for all gases in this study. An Applied Research TC-50 thermal gas cracker was employed to produce atomic hydrogen and was operated at 65 W, producing atomic hydrogen at an estimated 50% efficiency. The 1800 L dose consists of H_2(g) flowed for 30 min at a H_2 pressure of 1×10^{-6} Torr; note that the calculated Langmuirs do not include the H cracking fraction since this could not be experimentally determined so the reported atomic hydrogen Langmuirs are an upper limit. XPS was taken of the surface to determine the background carbon, oxygen, silicon, and germanium surface percentages prior to SiN_x deposition.

The high vacuum ALD (HV-ALD) dosing chamber (base pressure of 2×10^{-7} Torr) with attached precursor dosing lines was pumped by a turbomolecular pump backed by a dry pump, and the entire chamber, precursor dosing lines, and connecting line to the dry pump were heated by heat tape for 12 h at 125 °C. The manipulator was radiatively heated and outgassed in high vacuum by the PBN heater to 285 °C for 12 h. 12 h of preheating time was employed, and hot wall heating continued during ALD to ensure all stainless steel vacuum components reached the temperature of >100 °C, to prevent both precursors from sticking to adsorbates (H_2O, hydrocarbon, etc.) on the chamber walls and to eliminate the formation of the ammonium–chloride like powder byproduct, which formed with chamber walls at room temperature during ALD deposition. Subsequently, the sample was radiatively heated

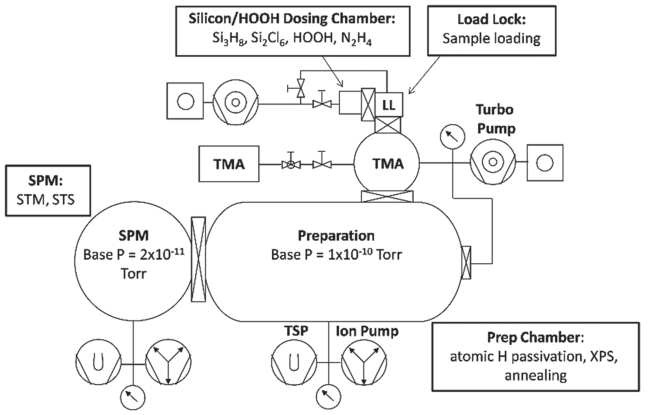

FIG. 1. Schematic diagram of the multichamber UHV/HV system where sample preparation and ALD deposition were performed.

to 285 °C for 15 min on the UHV manipulator in the prep chamber while simultaneously the HV-ALD chamber manipulator was also heated to 285 °C for 15 min to facilitate a faster sample transfer. The schematic of the multichamber UHV/HV system is shown in Fig. 1. The sample was transferred to the HV-ALD dosing chamber and 400 ML of N_2H_4 was dosed at a substrate temperature of 285 °C to terminate the surface with NH_x groups and prepare the surface for ALD. Next, 10–20 SiN_x ALD cycles were performed at a substrate temperature of 285 °C in order to deposit silicon nitride films of varying thickness on the Si_xGe_{1-x} surface. Each ALD cycle consisted of 13.5 ML Si_2Cl_6 (0.1 Torr dosed for 135 s) followed by 20 ML N_2H_4 (0.4 Torr dosed for 50 s) at a substrate temperature of 285 °C. The pressure during ALD processing was monitored by a convectron gauge, which showed peak spikes of 0.3 Torr and 1 Torr at the onset of Si_2Cl_6 and N_2H_4 doses; after each half-cycle dose, the chamber underwent a HV purge for 85 s to reduce the pressure to 5×10^{-5} Torr to ensure the removal of residual precursor from the deposition chamber before introduction of the next half-cycle. Anhydrous N_2H_4 was employed (Rasirc, Inc.), and prior to every new sample deposition, the N_2H_4 source container was recharged with 750 Torr of ultra-high purity N_2 to act as a carrier gas for delivery of N_2H_4 (vapor pressure of 15 Torr at 25 °C).

Following deposition, the sample was transferred back to the UHV preparation chamber and radiatively heated to 285 °C for 15 min and dosed with 1800 L of atomic hydrogen in order to remove any residual chlorine left in the deposited SiN_x film by inducing a HCl(g) desorption byproduct. The surface was subsequently characterized by XPS and transferred into the UHV SPM analysis chamber (base pressure of 2×10^{-11} Torr).

In the SPM chamber, scanning tunneling spectroscopy (STS) was performed to determine the electrical quality of the surface and probe the local surface density of states. Variable-z mode measurements were taken using an external lock-in amplifier with modulation signal (0.1 V_{ac}, 650 Hz) to directly obtain the dI/dV and I/V spectra by sweeping the sample bias from −2.5 to +2.5 V, and simultaneously moving the tip towards and then away from the surface.[27–29] An applied Δz initial offset ranging from −0.2 to −0.8 nm was used in order to maximize the I(V) signal without crashing the STM tip.

The raw I/V data are smoothed by a broadening function to create $\overline{I/V}$ using a low-pass filter with energy width of (3.0 eV)/2π (filter frequency parameter value of $(3.0\ \text{eV})^{-1}$), as described in previous studies.[30] The dI/dV spectra are normalized by dividing by $\overline{I/V}$.[30] The STS curves are reported by averaging 10-12 individual $(dI/dV)/(\overline{I/V})$ curves taken across the sample surface. These averaged curves are fitted (dashed red line in reported spectra) using a linear function described in previous STM/STS studies in order to extract the measured band edge energies of the plotted $(dI/dV)/(\overline{I/V})$ spectra, as band offsets contain linear dependence on sample bias.[30–32] The linear function fitting method contains slight rounding at the band gap onset due to temperature and AC modulation. Standard errors are obtained by the fitting process and reported for averaged STS curves. The uncertainties provided by the fitting method are statistical uncertainties using the least squares fitting,[32] and these reported uncertainties are much less than thermal broadening in STS measurements.

After SiN_x deposition, the samples were taken out of UHV and placed under 750 Torr ultra-high purity N_2 until ready for MOSCAP fabrication. Capacitance-voltage (C-V) characterization of SiN_x/SiGe interfaces was performed by fabrication of HfO_2/SiN_x/SiGe metal-oxide-semiconductor capacitors (MOSCAPs). HfO_2 ALD was performed at 300 °C in the Beneq TFS-200 continuous flow reactor using Ar carrier gas, with 40 sequential pulses of $HfCl_4$ (500 ms) and H_2O (500 ms). After each precursor pulse, a 6 s long Ar purge was employed. Following HfO_2 ALD, Ni gate metal and Al back contacts were deposited by thermal evaporation and DC sputtering, respectively. After HfO_2 and metal gate and back contact deposition, the MOSCAPs underwent a 15 min forming gas anneal in 5% H_2/N_2. C-V were measured at variable frequencies ranging from 2 kHz to 1 MHz with AC modulation amplitude of 30–50 mV and DC bias range of −2 to 2 V. By fitting the frequency dispersion of C-V and conductance-voltage (G-V) responses around the depletion region and inversion region, the density of interface traps at various energy levels relative to the edge of the valence band was calculated using the full interface state model, which consists of a Δ circuit of three complex elements to represent charge trapping by interface traps.[33,34]

All DFT simulations were performed by VASP plane-wave DFT package using projector augmented-wave (PAW) pseudopotentials (PP), PBE-GGA exchange-correlation functional for DFT-MD, and more accurate HSE06 hybrid-functional for the final electronic structure calculations.[35–44]

The first step in the density-functional theory (DFT) simulations was modeling a-$SiO_{0.8}N_{0.8}$ and a-Si_3N_4 interlayers on SiGe(001). The SiGe substrate was a 2 × 2 × 3 SiGe supercell using lattice constants which were DFT-relaxed at variable volume. The 3 bottom layers were permanently fixed in bulk-like positions and passivated by relaxed H atoms to simulate continuous bulk. The upper surface of the SiGe slab was Si-terminated. The larger 2 × 2 surface area of the supercell provides more realistic amorphous interlayer/SiGe simulations than the 1 × 1 SiGe unitcell surface area. Due to high computational cost of DFT molecular dynamics (MD) simulations, the largest supercell was chosen which could provide a reasonable simulation time. The 2 × 2 × 3 SiGe supercell had 96 atoms, while the a-HfO_2 sample had 120 atoms. In addition, around 20 passivating H atoms and around 20 interlayer O/N atoms were included to the system resulting in roughly 250

atoms in total. Furthermore, the SiGe slab and a-HfO_2 sample should have a thickness around 10 Å or higher to have bulk-like properties. With these constraints, the 2 × 2 supercell surface area was the most computationally affordable. Switching to a greater 3 × 3 surface area would have made the whole a-HfO_2/interlayer/SiGe stack too large for computationally affordable DFT-MD simulations. The a-$SiO_{0.8}N_{0.8}$ and a-Si_3N_4 interlayers were formed by DFT molecular dynamics (DFT-MD) in 2 stages.

To form the a-$SiO_{0.8}N_{0.8}$ interlayer, initially 8 Si, 7 O, and 7 N atoms were added randomly on the surface resulting together with 8 surface Si atoms in 16 Si, 7 O, and 7 N atoms. The stack was annealed at 800 K for 1000 fs, cooled to 0 K for 200 fs, and relaxed to the ground state with the conjugate-gradient relaxation algorithm.[45] This formed the "Si-rich sub-stoichiometric" layer of a-$SiO_{0.8}N_{0.8}$ (or a-$SiO_{0.4}N_{0.4}$). Since DFT-MD is a computationally expensive technique, the simulated time scale for systems of 100-300 atoms is typically limited to picoseconds (~1 fs time-step) to have a reasonable run time. Using a higher annealing temperature accelerates kinetic processes and effectively elongates the simulated time scale. The 800 K annealing temperature was chosen to be lower than the melting temperature of the SiGe stack. The melting temperature for Ge is 1210 K, for Si is1685 K, and for $Si_{0.5}Ge_{0.5}$ it is estimated to be1382 K.[46] The DFT-MD temperature 800 K was chosen to be lower than 1382 K because of two reasons: (i) the DFT melting temperature can be lower than the experimental one; (ii) having an annealing temperature above 800 K often causes deposited O/N atoms to leave the surface. To form the stoichiometric interlayer, an additional 6 O and 6 N atoms were added in a random manner to the previous surface resulting in a total of 16 Si, 13 O, and 13 N atoms. This stack was again annealed at 800 K for 1000 fs, cooled to 0 K for 200 fs, and relaxed to the ground state with the conjugate-gradient relaxation algorithm giving the "stoichiometric" layer of a-$SiO_{0.8}N_{0.8}$.

The a-Si_3N_2 and a-Si_3N_4 interlayers on SiGe(001) were formed in a similar manner. Originally, 8 Si and 11 N atoms were added randomly on the surface resulting together with 8 surface Si atoms in 16 Si and 11 N atoms. The slab was DFT-MD annealed, cooled, and relaxed as described previously forming a Si-rich sub-stoichiometric layer of a-Si_3N_2. At the second stage, 10 more N atoms were added in a random manner to the previous surface resulting in 16 Si, 21 N atoms and DFT-MD annealed, cooled, relaxed as described previously forming a fully stoichiometric layer of a-Si_3N_4.

The high-quality model of a-HfO_2 was generated for the SiGe(001) substrate area using the "melt-and-quench" approach by using DFT-MD at finite temperature described in detail elsewhere.[47–50] The amorphous a-HfO_2 sample was selected from a batch of 10 DFT-MD samples with different simulation parameters and compared against reference experimental and calculated properties such as coordination distribution, bandgap, average coordination numbers, radial-distribution functions (RDF's), and others to ensure high sample realism and absence of defects. The amorphous samples were generated to fit the SiGe(001) substrate cross-sectional area. The selected amorphous bulk sample was cut to create surfaces before stacking to the interlayer/SiGe substrate.

The selected a-HfO_2 sample was stacked on the previously simulated a-$SiO_{0.4}N_{0.4}$, a-$SiO_{0.8}N_{0.8}$, a-Si_3N_2, and a-Si_3N_4 interlayers on SiGe(001) resulting in stacks. Each stack was annealed at 800 K for 2000 fs, the total energy of the stack was analyzed from 1000 fs to 2000 fs of annealing and 4 points of low energy were detected. Starting from these 4 low energy points, the stack was cooled to 0 K for 200 fs and relaxed to the ground state with conjugate-gradient relaxation algorithm and force-tolerance level of 0.05 eV/Å generating 4 final stacks. Among these 4 final stacks the stack with the lowest final total energy was identified and used. For a-HfO_2/a-Si_3N_2/SiGe, the selected annealing time was 1919 fs while for a-HfO_2/a-Si_3N_4/SiGe it was 1989 fs. For a-HfO_2/a-$SiO_{0.4}N_{0.4}$/SiGe the selected annealing time was 1836 fs, while for a-HfO_2/a-$SiO_{0.8}N_{0.8}$/SiGe it was 1930 fs. Since the standard PBE exchange-correlation functional underestimates semiconductor bandgaps, the simulated stacks were rescaled from PBE to HSE06 SiGe lattice constants (different by several %) and accurate electronic structure including density of states and band-decomposed charge density was calculated with the HSE06 functional.[39–41]

III. RESULTS AND DISCUSSION

XPS was employed in order to determine the ALD saturation pulses of Si_2Cl_6 and N_2H_4 at 285 °C on $Si_{0.5}Ge_{0.5}$(110) and $Si_{0.7}Ge_{0.3}$(001) surfaces. Fig. 2(a) shows the $Si_{0.5}Ge_{0.5}$(110) corrected XPS peak areas of Si 2p (both the total Si 2p peak area and the higher binding energy shoulder of Si 2p are shown), Ge 3d, O 1s, C 1s, N 1s, and Cl 2p normalized to the sum of the total (shifted and unshifted) Si 2p and total Ge 3d signals for the as-loaded wet cleaned $Si_{0.5}Ge_{0.5}$(110) surface, and following an 1800 L atomic hydrogen dose at 330 °C, 400 ML N_2H_4 dose at 285 °C, 1X Si_2Cl_6 dose at 285 °C (13.5 ML), 3X additional Si_2Cl_6 dose at 285 °C (40.5 ML), 1X N_2H_4 dose at 285 °C (20 ML), and 3X N_2H_4 dose at 285 °C (60 ML). Both the $SiCl_x$ and NH_x coverages reach near saturation coverage following a 1X dose indicating an ALD process occurs at 285 °C as seen by a negligible increase in Si 2p or N 1s corrected peak areas with increased dosing times.

Fig. 2(b) shows the corrected XPS peak areas normalized to the sum of total Si 2p and total Ge 3d signal on the $Si_{0.7}Ge_{0.3}$(001) surface following an 1800 L atomic hydrogen dose at 330 °C, 400 ML N_2H_4 dose at 285 °C, 1X Si_2Cl_6 dose at 285 °C (13.5 ML), 3X additional Si_2Cl_6 dose at 285 °C (40.5 ML), 1X N_2H_4 dose at 285 °C (20 ML), and 3X N_2H_4 dose at 285 °C (60 ML). Similar to the $Si_{0.5}Ge_{0.5}$(110) case, both the $SiCl_x$ and NH_x coverages reach near saturation following a 1X dose, consistent with an ALD process. It is noted that for even the first 1-2 monolayers of SiN_x, the Si/N ratio is independent of crystal face.

These surface sensitive XPS spectra show that the hydrogen cleaned $Si_{0.5}Ge_{0.5}$(110) surface contains ~63% germanium while the hydrogen cleaned $Si_{0.7}Ge_{0.3}$(001) surface contains ~38% germanium. Small amounts of carbon (<~5%) and oxygen (<~10%) detected on both the SiGe(001) and (110) surfaces remain following the initial wet cleaning procedure and the *in situ* atomic H dry cleaning due to adsorption of oxygen containing hydrocarbons onto surface silicon from the

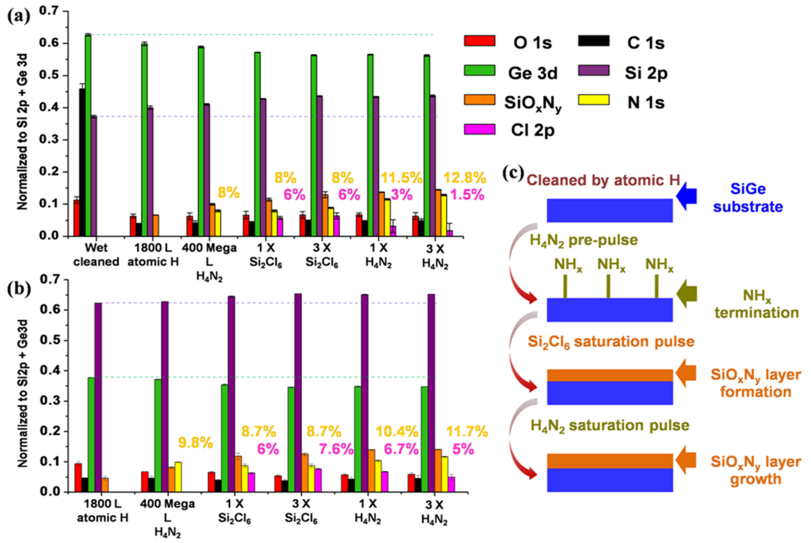

FIG. 2. XPS of ALD saturation on $Si_{0.5}Ge_{0.5}(110)$ and $Si_{0.7}Ge_{0.3}(001)$. (a) $Si_{0.5}Ge_{0.5}(110)$ and (b) $Si_{0.7}Ge_{0.3}(001)$. XPS corrected peak areas of Si 2p (both the total Si 2p peak area and the higher binding energy component of Si 2p), Ge 3d, O 1s, C 1s, N 1s, and Cl 2p are normalized to the sum of all Si 2p and Ge 3d peaks. Compositions based on XPS are shown following an 1800 L atomic hydrogen dose at 330 °C, 400 ML N_2H_4 dose at 285 °C, 1X Si_2Cl_6 dose (13.5 ML) at 285 °C, 3X additional Si_2Cl_6 dose (40.5 ML) at 285 °C, 1X N_2H_4 dose (20 ML) at 285 °C, and 3X N_2H_4 dose (60 ML) at 285 °C. The percent nitrogen is indicated in gold and percent chlorine in magenta. Note that the typical as-loaded wet cleaned $Si_{0.7}Ge_{0.3}(001)$ shows 40%–50% carbon on the surface. (c) Schematic diagram showing the SiGe(001)/(110) surface atomic hydrogen cleaning, initial N_2H_4 prepulsing, and ALD half cycle surface reactions.

brief air exposure occurring during the sample transfer into high vacuum and the 330 °C atomic hydrogen cleaning.[51] Following a 1X dose of N_2H_4, the $Si_{0.5}Ge_{0.5}(110)$ surface contains less than half the amount of residual chlorine on the surface as compared with the $Si_{0.7}Ge_{0.3}(001)$ surface, consistent with Si–Cl surface species being more thermodynamically stable than Ge–Cl species, and a germanium rich SiGe substrate undergoing silicon surface segregation in the presence of chlorine surface termination at 275 °C.[52] Both the $Si_{0.5}Ge_{0.5}(110)$ and $Si_{0.7}Ge_{0.3}(001)$ surfaces contain residual chlorine following one complete ALD reaction cycle due to the strong N–H (431 kJ/mol) and Si–Cl (377 kJ/mol) bonds making it difficult to produce the HCl(g) desorption byproduct at a low deposition temperature.[53]

Figs. 3(a)–3(c) show the raw XPS peak areas for Si 2p, N 1s, and Ge 2p peaks on the as-loaded wet cleaned $Si_{0.5}Ge_{0.5}(110)$ surface following an 1800 L atomic hydrogen dose at 330 °C, an additional 400 ML N_2H_4 dose at 285 °C, and following an additional 20 SiN_x ALD cycles at 285 °C. The large shifted Si 2p peak (~68% of the total Si 2p signal) indicative of SiO_xN_y is located at a binding energy of 101.7 eV, and the N 1s peak is located at 397.7 eV. A small

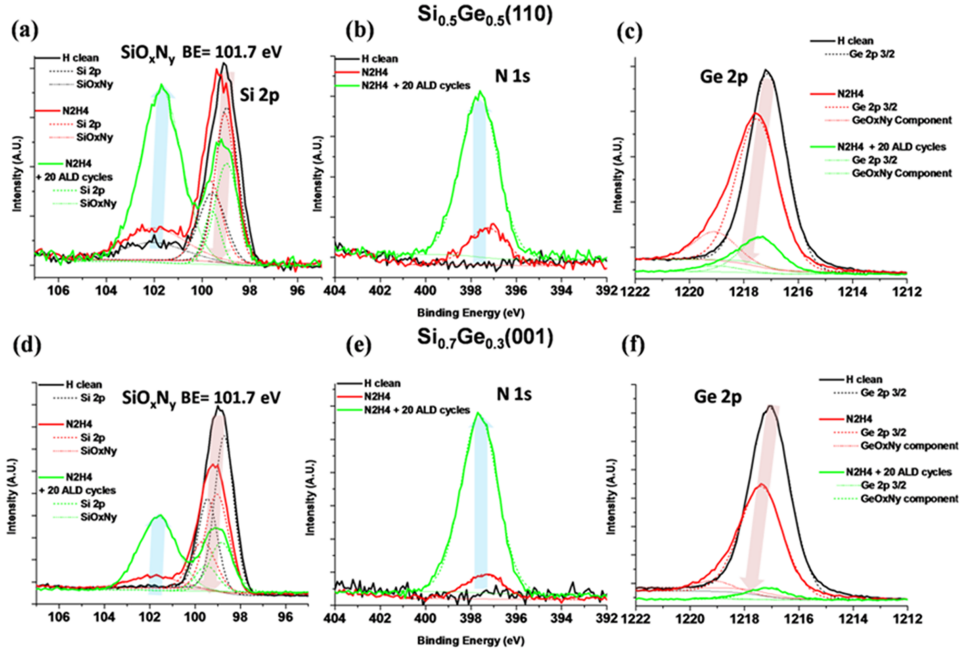

FIG. 3. XPS spectra of $Si_{0.5}Ge_{0.5}(110)$ and $Si_{0.7}Ge_{0.3}(001)$ after ALD with $N_2H_4(g)$ and $Si_2Cl_6(g)$. (a)–(c) XPS of ALD on $Si_{0.5}Ge_{0.5}(110)$; and (d)–(f) XPS of ALD on $Si_{0.7}Ge_{0.3}(001)$. XPS fitted raw peak areas are shown for Si 2p, N 1s, and Ge 2p peaks on the as-loaded wet cleaned SiGe surfaces following an 1800 L atomic hydrogen dose at 330 °C, an additional 400 ML N_2H_4 dose at 285 °C, and an additional 20 SiN_x ALD cycles of $Si_2Cl_6(g)$ and $N_2H_4(g)$ at 285 °C.

higher binding energy Ge 2p component is seen at 1219.1 eV indicative of GeO_xN_y surface bonding after the N_2H_4 dose, with slightly more nitrogen found bonded to silicon (25% of Si 2p total corrected peak area signal) than nitrogen bonded to germanium (15% of Ge 2p total corrected peak area signal) as predicted by the large silicon and germanium nitride formation enthalpy differences of −177 and −15 kcal/mol.[54] Following the 20 SiN_x ALD cycles, the intensity of the Ge 2p signal decreases by a factor of 5 indicating that Ge–N bonds are localized at the SiO_xN_y/SiGe interface.

Similar results are shown on the as-loaded wet cleaned $Si_{0.7}Ge_{0.3}$(001) (Figs. 3(d)–3(f)). After the initial N_2H_4 dose, the large shifted SiO_xN_y peak, located at 101.7 eV, makes up ~60% of the total Si 2p signal on $Si_{0.7}Ge_{0.3}$(001), and the N 1s peak is located at 397.7 eV. After the initial N_2H_4 dose, the GeO_xN_y surface high binding energy component, located at binding energy 1219.1 eV, makes up ~15% of the total Ge 2p signal on the $Si_{0.7}Ge_{0.3}$(001) surface. Following an additional 20 SiN_x ALD cycles, the intensity of the Ge 2p signal decreases by a factor of 10 on $Si_{0.7}Ge_{0.3}$(001) showing that on both higher and lower Ge content SiGe(001)/(110) surfaces the SiO_xN_y thin film provides a protective diffusion barrier preventing Ge out diffusion to the surface. The results on the 50% SiGe(001) surface are similar to 30% SiGe(001) (see the supplementary material). ~10% oxygen was found following 20 SiN_x ALD cycles on SiGe(001) and (110) from the residual oxygen remaining on the SiGe surfaces following the initial atomic hydrogen cleaning, and from a small amount of residual background H_2O found inside the ALD chamber. The heat for the formation of SiO_2 (−911 kJ/mol) is 3.7 times great per silicon atom than the heat of formation for Si_3N_4 (−744 kJ/mol or −248 kJ/mol-silicon). Therefore, at equilibrium trace amount of H_2O or O_2 can result in formation for SiON instead of SiN_x.[55]

The XPS corrected peak areas were normalized to the sum of the unshifted Si 2p and Ge 3d peaks as shown in Fig. 4 to more clearly illustrate the nitride film growth and for quantification of the film thickness and stoichiometry. These substrate normalized XPS ratios are shown following an 1800 L atomic hydrogen dose at 330 °C, an additional 400 ML N_2H_4 dose at 285 °C, 20 SiN_x ALD cycles at 285 °C, and a final 1800 L atomic hydrogen dose at 285 °C on $Si_{0.5}Ge_{0.5}$(110), $Si_{0.5}Ge_{0.5}$(001), and $Si_{0.7}Ge_{0.3}$(001) surfaces. The final atomic hydrogen dose was employed after 20 ALD cycles in order to reduce residual chlorine species in the deposited film. The equation $\ln(I/I_o) = -t/\lambda$ was used to calculate the estimated deposited SiN_x film thickness, where I is the intensity of the sum of unshifted Si 2p and Ge 3d peaks following the N_2H_4 dose and 20 SiN_x ALD cycles, I_o is the intensity of the sum of unshifted Si 2p and Ge 3d peaks following the N_2H_4 dose, "t" is the thickness of the deposited SiN_x layer, and λ is the inelastic mean free path of the Si 2p and Ge 3d collected electrons (2.2 nm).[56] The thickness is multiplied by cosine of the emission angle (60°) to account for the glancing angle (30°) of detection. The deposited film is estimated to be a thin silicon rich SiN_x film of ~0.4 nm thickness on the $Si_{0.5}Ge_{0.5}$(110) surface, and ~0.6 nm thickness on the $Si_{0.5}Ge_{0.5}$(001) and $Si_{0.7}Ge_{0.3}$(001) surfaces.

The stoichiometry of the deposited film was calculated by comparing the actual amount of silicon in a shifted oxidation state detected in the SiON to the theoretical amount of silicon that would be in a shifted oxidation state if the SiON was stoichiometric. The amount of "stoichiometric" SiO_xN_y is calculated (a) from the amount of O and N after subtracting the small amount of GeON and (b) assuming the oxidized Si is in an alloy of SiO_2 and Si_3N_4 to calculate the percentage of silicon in stoichiometric SiO_xN_y,

$$\begin{aligned}\text{Stoichiometric } SiO_xN_y &= Si_{x/2+3y/4}O_xN_y \\ &= 0.5^*(\text{O XPS peak}) \\ &\quad + 0.75^*(\text{N XPSpeak} \\ &\quad - \text{shifted Ge XPS peak}). \end{aligned} \tag{1}$$

If there is Si rich silicon sub-oxynitride, then the experimental XPS Si signal from $SiO_xN_y \gg$ calculated Si in ideal

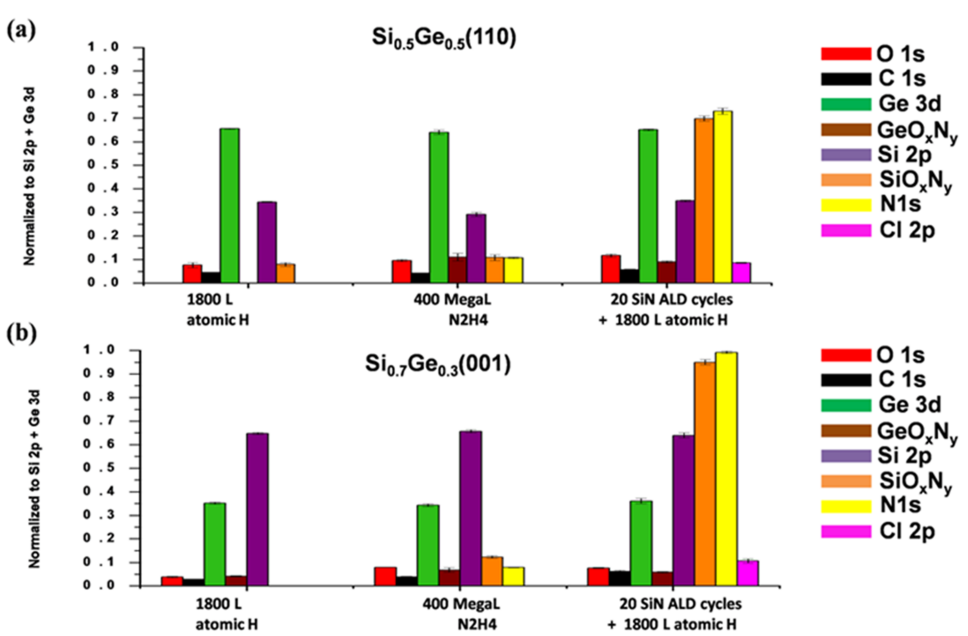

FIG. 4. XPS derived surface compositions of $Si_{0.5}Ge_{0.5}$(110) and $Si_{0.7}Ge_{0.3}$(001) after ALD with N_2H_4(g) and Si_2Cl_6(g). (a) $Si_{0.5}Ge_{0.5}$(110), (b) $Si_{0.7}Ge_{0.3}$(001) XPS corrected peak areas of unshifted Si 2p, unshifted Ge 3d, SiO_xN_y, GeO_xN_y, O 1s, C 1s, N 1s, and Cl 2p normalized to the sum of unshifted Si 2p and unshifted Ge 3d peaks following an 1800 L atomic hydrogen dose at 330 °C, 400 ML N_2H_4 dose at 285 °C, and following an additional 20 SiN_x ALD cycles and final atomic hydrogen dose at 285 °C.

stoichiometric $SiO_xN_y = Si_{x/2+3y/4}O_xN_y$ from Eq. (1). Note that the calculated SiO_xN_y from Eq. (1) does not account for surface carbon and residual chlorine species bonding to silicon.

Fig. 4 shows the amounts of oxygen, nitrogen, and oxidized silicon and germanium species on the $Si_{0.5}Ge_{0.5}(110)$ (a) and $Si_{0.7}Ge_{0.3}(001)$ (b) surfaces after 20 ALD cycles. The results on $Si_{0.5}Ge_{0.5}(001)$ are very comparable to $Si_{0.7}Ge_{0.3}(001)$, and can be found in the supplementary material. It is assumed that all GeO_xN_y is substoichiometric GeN due to the small chemical shift found on surface Ge and because oxygen initially bonds only to silicon. The XPS signals shown in Fig. 4 do not account for variation in film thicknesses or the depth distributions of O, N, and shifted Si species. For $Si_{0.5}Ge_{0.5}(110)$, using Eq. (1) if all the SiON was stoichiometric (i.e., a mixture of SiO_2 and Si_3N_4) then the shifted Si peak should be 0.56, which is equal to the calculated stoichiometric SiO_xN_y from Eq. (1); however, the experimental shifted Si is 0.70, therefore the real SiO_xN_y is 25% silicon rich (0.70/0.56 = 1.25). On $Si_{0.7}Ge_{0.3}(001)$, if all the SiON was stoichiometric (Eq. (1)), then SiO_xN_y should equal 0.75, while the shifted Si XPS peak is 0.95 indicating the film is 26% silicon rich. As shown below in the DFT calculations, a silicon rich SiO_xN_y may be beneficial since it minimizes the formation of Ge–N and Ge–O bonds.

20 ALD cycles on 30% Ge SiGe(001) and 50% Ge SiGe(001)/(110) surfaces leave a substoichiometric silicon rich SiO_xN_y film where it is hypothesized that residual Si–Cl and trace Si–O species in the thin deposited film serve to block nitrogen from fully nitriding silicon to stoichiometric Si_3N_4. The SiO_xN_y peak is located at binding energy 101.7 eV on all SiGe(001)/(110) surfaces. Stoichiometric amorphous Si_3N_4 has a binding energy of 102 eV[57] and stoichiometric SiO_2 has a binding energy of 104 eV[58] making the measured binding energy in these films consistent with a silicon rich SiO_xN_y film predominantly made of SiN_x.

STS measurements probing the local surface density of states of the SiO_xN_y/SiGe surface were performed at room temperature as shown in Figures 5(a)–5(f). Bilinear fits are shown in Fig. 5 (dotted blue and pink lines) so that band edge states are properly fitted; however, for the discussion of the bandgap size, the outer bandgap is reported and, therefore, represents the full bandgap in the presence of band edge states. Therefore, the estimate of the band gaps does not include the VB and CB edge states observed in the narrow band gap spectra or the VB band edge states observed in the wide band gap regions. States outside the bandgap of SiGe and near the SiGe band edges are best evaluated with MOSCAP measurements. The $Si_{0.5}Ge_{0.5}(110)$ surface contains the thinnest deposited film (~0.4 nm from XPS data) and has the largest range of measured band gap energies with 60% of the curves containing a larger band gap of ~1.4 ± 0.02 eV (Fig. 5(a)), and 40% showing a narrow band gap (~1.0 ± 0.02 eV) (Fig. 5(d)) more reflective of the SiGe substrate, indicating the presence of varying nitride stoichiometry across the surface after the initial 1-3 monolayers of SiN_x nucleation and growth on the surface. It is hypothesized that the SiO_xN_y ALD nucleation on the (110) surface is more difficult because this surface contains smaller domains and increased disorder and roughness, as previously shown in STM and STS studies comparing SiGe(001)/(110) surfaces.[59] The narrow SiN_x band gap (1–1.6 eV) has been previously reported for subnanometer SiN_x films on Si(001) surfaces by STS measurements at both low and high deposition temperatures.[60,61]

It has been reported that when subnanometer SiN_x films are deposited at low temperatures (<600 °C), SiN_x grows in a layer by layer fashion and silicon and nitrogen atoms are limited in diffusion across the surface and tend to form incomplete non-stoichiometric Si_3N_4 in which the N atoms have less than three bonds to Si.[60] The $Si_{0.5}Ge_{0.5}(001)$ contains a thicker deposited SiO_xN_y film (~0.6 nm by XPS) with 90% of the surface curves showing a measured averaged band gap of 2.1 ± 0.02 eV (Fig. 5(b)), and 10% of the curves showing an averaged narrow band gap (1.1 ± 0.17 eV) (Fig. 5(e)). Similarly on the $Si_{0.7}Ge_{0.3}(001)$ surface with ~0.6 nm

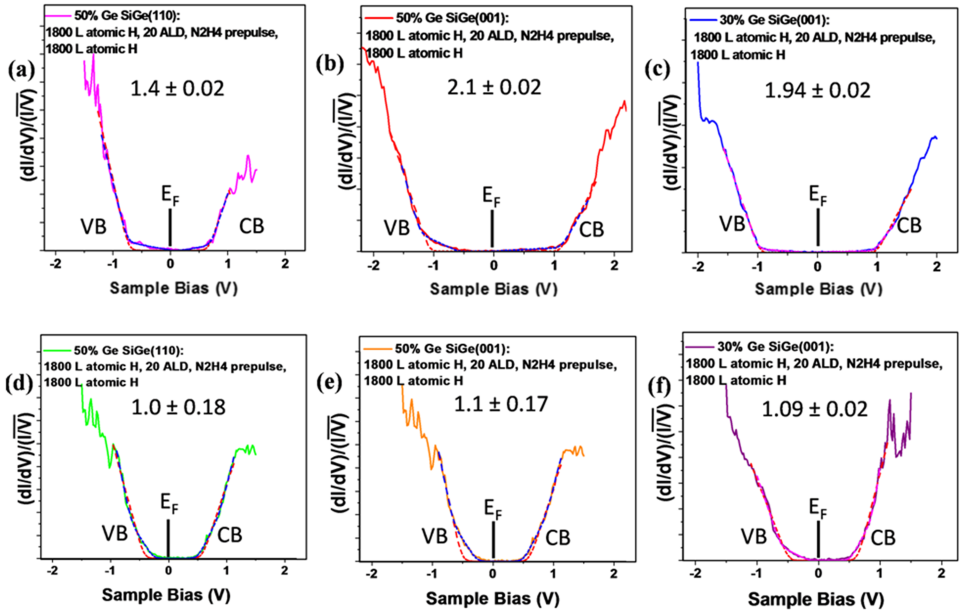

FIG. 5. STS of $Si_{0.5}Ge_{0.5}(110)$, $Si_{0.5}Ge_{0.5}(001)$, $Si_{0.7}Ge_{0.3}(001)$ after N_2H_4 + Si_2Cl_6 ALD. STS on (a) and (d) p-type $Si_{0.5}Ge_{0.5}(110)$, (b) and (e) p-type $Si_{0.5}Ge_{0.5}(001)$, (c) and (f) p-type $Si_{0.7}Ge_{0.3}(001)$ following an 1800 L atomic H dose at 330 °C, an additional 400 ML N_2H_4 dose at 285 °C, an additional 20 SiN_x ALD cycles at 285 °C, and a final 1800 L atomic H dose at 285 °C. Both narrow and wider band gap curves are measured across all surfaces and are reported here. Note the absence of band gap trap states indicative of surface passivation.

SiO_xN_y film measured by XPS, 90% of the surface curves show a measured averaged band gap of 2.1 ± 0.02 eV (Fig. 5(c)), and 10% show an averaged narrow band gap (1.09 ± 0.02 eV) (Fig. 5(f)). Note that for all surfaces, the absence of midgap states is indicative of surface passivation without formation of unwanted trap defect states. It is hypothesized that with increasing deposited film thickness, the band gap increases towards that expected for a stoichiometric Si_3N_4 film. Because this work focuses on depositing a thin subnanometer film to passivate the SiGe(001)/(110) surface and protect against germanium out-diffusion, thicker film properties were not investigated. The narrow bandgaps on 10% of the (001) surfaces were not considered an issue since during ALD gate oxide deposition and post deposition anneal, the interfacial silicon will become fully oxidized and, therefore, the interlayer will have a wide bandgap as shown below by the lower gate leakage for devices formed on the N_2H_4 + Si_2Cl_6 samples.

Following XPS and STS, MOSCAPs were fabricated with and without the insertion of the SiO_xN_y layer on both $Si_{0.7}Ge_{0.3}$(001) and $Si_{0.5}Ge_{0.5}$(001) prior to HfO_2 deposition to investigate the electronic structure of the SiO_xN_y/SiGe interfaces. To deposit a thin SiO_xN_y diffusion barrier and still maintain a low EOT, 10-15 cycles of SiN_x ALD (with estimated thickness of 0.2–0.3 nm) were employed. In order to determine if more highly silicon enriched SiN_x film would improve the interface quality, a second SiN_x recipe with half the N_2H_4 pulse length per ALD cycle was explored for MOSCAP fabrication. MOSCAPs were fabricated following 20 SiN_x ALD cycles with half the N_2H_4 pulse length per cycle, so that the SiN_x film thickness would be comparable to that from the regular recipe (~0.2–0.3 nm).

Fig. 6 shows the C-V characteristics of HfO_2/$Si_{0.7}Ge_{0.3}$(001) MOSCAPs fabricated following cyclic HF clean (a), 20 cycles of SiN_x ALD with 10 ML N_2H_4 pulses per cycle (b), and 10 cycles of SiN_x ALD with 20 ML N_2H_4 pulses per cycle (c). The C-V characteristics were measured for 6 MOSCAPs for each condition shown in (a)–(c). Although the device with HF clean has a higher maximum capacitance in accumulation (C_{max}), it also has a large interface trap feature (known as the D_{it} bump) observed near the flat band region. In comparison, MOSCAPs with a SiN_x interfacial layer (Figs. 6(b) and 6(c)) showed smaller D_{it} bumps as well as smaller C_{max}. The lower C_{max} is consistent with the SiO_xN_y layer having a sufficient band gap to prevent the accumulation of electrons in the SiO_xN_y layer. Moreover, addition of SiN_x at the interface improved the gate leakage characteristics by lowering the maximum gate leakage in accumulation by almost an order of magnitude (Fig. 6(d)). While the two MOSCAPs with SiN_x layers have similar C_{max} values, 10 cycles of SiN_x ALD with the longer N_2H_4 pulse resulted in smaller D_{it} bump (Fig. 6(c)) and lower gate leakage (Fig. 6(d)), indicating that the SiN_x ALD recipe with full saturation of the N_2H_4 pulse leads to a better interface quality with less chlorine and more nitrogen in the film; note that this interlayer is still Si rich (i.e., substoichiometric) compared to a mixture of SiO_2 and Si_3N_4.

Using the full interface state model for quantitative analysis of the C-V and G-V characteristics, D_{it} versus Fermi energy level (relative to the edge of the valence band) profiles have been extracted for the three above-mentioned MOSCAPs (Fig. 7). By employing SiN_x ALD, the detectable D_{it} distribution energy range has decreased from 0.15 to 0.65 eV for the HF cleaned sample to 0.15-0.51 eV for 20 cycles of SiN_x, and 0.15–0.45 eV for 10 cycles of SiN_x.

The lower D_{it} comes at the expense of an increase in the equivalent oxide thickness (EOT) as shown in Fig. 7(b).

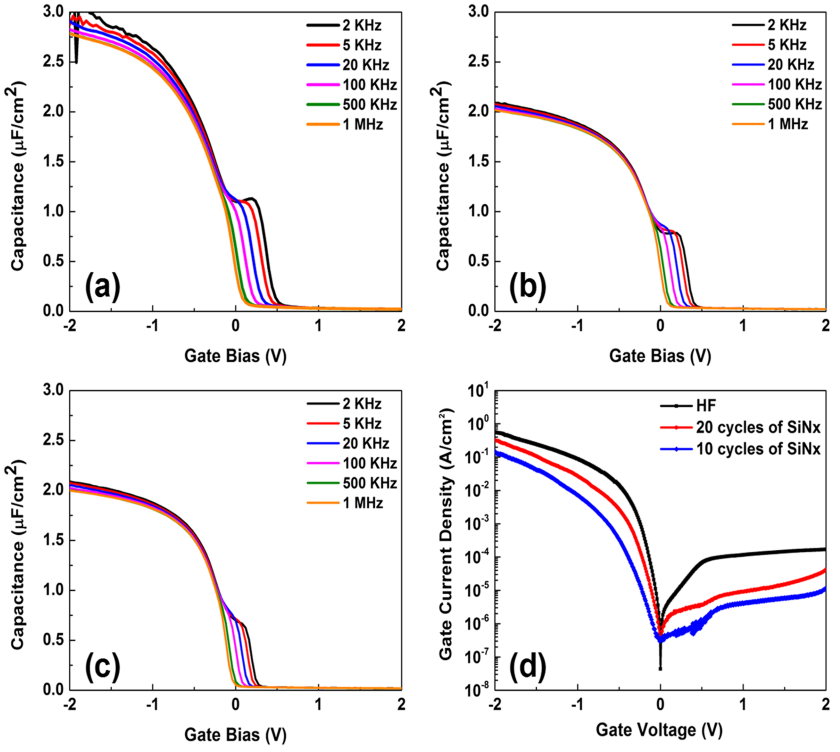

FIG. 6. C-V characteristics of $Si_{0.7}Ge_{0.3}$(001) MOSCAPs with 40 cycles of HfO_2 deposited by ALD. C-V curves after (a) HF cyclic clean; (b) 20 cycles of SiN_X ALD with 10 ML N_2H_4 pulse length per cycle; (c) 10 cycles of SiN_X ALD with 20 ML N_2H_4 pulse length per cycle. Gate leakage characteristics of the three MOSCAPs are shown in (d).

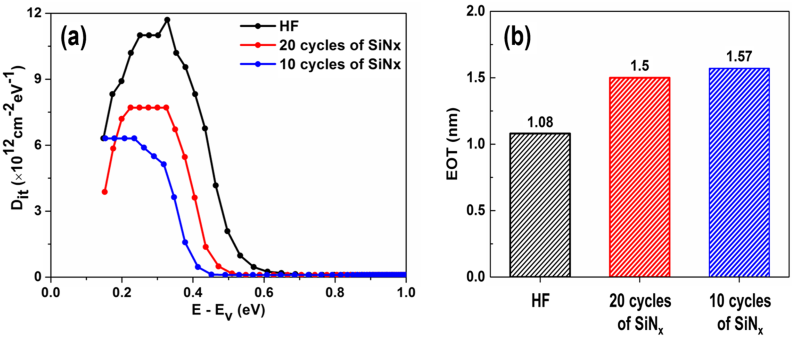

FIG. 7. Density of interfacial trap states (D_{it}) and equivalent oxide thicknesses (EOT) for $Si_{0.7}Ge_{0.3}$ MOSCAPs with 40 cycles of HfO_2 deposited by ALD: (a) D_{it} vs. E_F–Ev for HF cyclic clean, 20 cycles of SiN_x ALD, and 10 cycles of SiN_x ALD with 2x longer N_2H_4 pulses. (b) EOT values for HF cyclic clean, 20 cycles of SiN_x ALD, and 10 cycles of SiN_x ALD with 2x longer N_2H_4 pulses.

Relative to the HF cleaned sample, ALD deposition of SiN_x resulted in a 0.5 nm EOT increase for 10 ALD cycles with 10 ML N_2H_4 pulses per cycle and 0.57 nm increase for 20 ALD cycles with 20 ML N_2H_4 pulses per cycle. Note that this increase in EOT is greater than expected from the deposition of 0.2 nm to 0.3 nm of SiN_x; the increased EOT results partially from the deposition of silicon-rich SiN_x, but primarily from the air exposure after SiN_x deposition and before gate oxide ALD. The SiN_x passivated surfaces may also increase the nucleation of HfO_2, leading to a thicker deposited HfO_2 film. It is hypothesized that device fabrication without an air exposure after SiN_x deposition would create a lower total EOT than the reported results. The results shown are consistent with SiN_x ALD forming an SiON interfacial layer between HfO_2 and $Si_{0.7}Ge_{0.3}$(001), with bonding states that reduce D_{it} by almost 2x with an EOT increase of just 0.50–0.57 nm.

Fig. 8 displays the C-V characteristics of HfO_2/$Si_{0.5}Ge_{0.5}$(001) MOSCAPs fabricated on surfaces with and without SiN_x interfacial layers. Due to low substrate doping and consequently large series resistance, high levels of frequency dispersion in accumulation were observed for $Si_{0.5}Ge_{0.5}$(001) MOSCAPs. Therefore, only the low-frequency C-V characteristics (up to 20 kHz) are shown. Relative to the MOSCAPs with cyclic HF clean (Fig. 8(a)), addition of SiN_x to the interface (Figs. 7(b) and 7(c)) led to lower C_{max}, a smaller D_{it} bump, and similar gate leakage in accumulation (Fig. 6(d)). 20 cycles of SiN_x with 10 ML N_2H_4 pulse length per cycle (Fig. 8(b)) contains a larger D_{it} bump, and an increased false inversion component (observed for 1 V < Vg < 2 V) in comparison with 15 cycles of SiN_x ALD with 20 ML N_2H_4 pulse lengths per cycle (Fig. 8(c)). In addition, the longer N_2H_4 pulse length nearly eliminated the false inversion capacitance caused by large density of interface traps closer to the edge of the conduction band of $Si_{0.5}Ge_{0.5}$(001). Therefore, a fully saturating N_2H_4 pulse during SiN_x ALD results in a better passivation layer on the $Si_{0.5}Ge_{0.5}$(001) surfaces consistent with the need for a more nitrogen rich film to reduce Ge out-diffusion for the higher Ge content $Si_{0.5}Ge_{0.5}$(001) substrates; note that this interlayer is still Si rich (i.e., substoichiometric) compared to a mixture of SiO_2 and Si_3N_4.

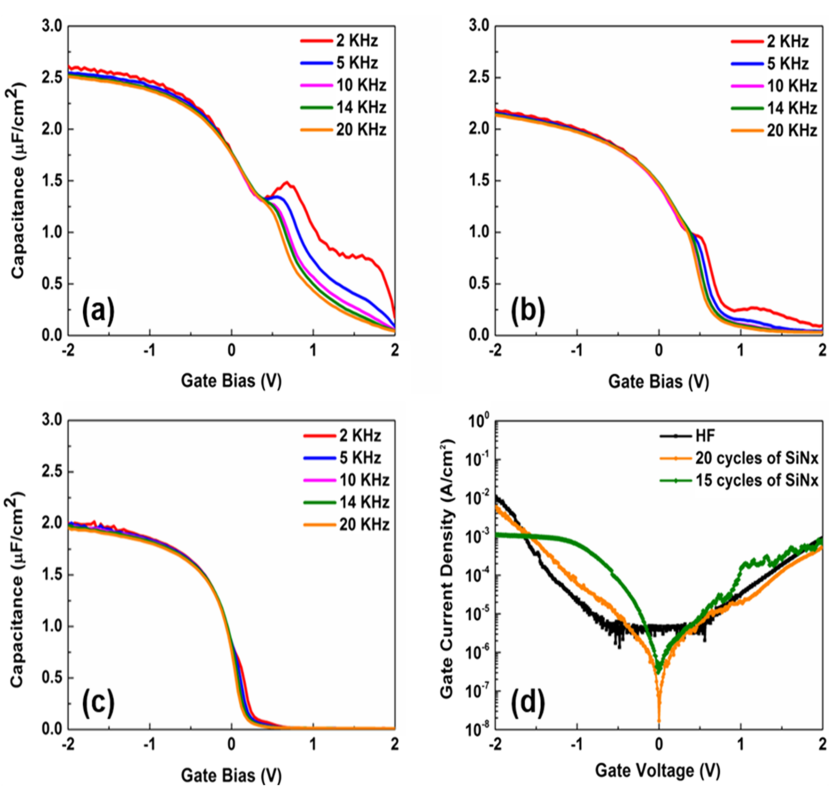

FIG. 8. C-V characteristics of $Si_{0.5}Ge_{0.5}$(001) MOSCAPs with 40 cycles of HfO_2 deposited by ALD: C-V spectra of: (a) HF cyclic clean; (b) 20 cycles of SiN_x ALD (10 ML N_2H_4 pulse length); (c) 15 cycles of SiN_x ALD with 2x longer N_2H_4 pulses (20 ML N_2H_4 pulse length). Note: Due to low substrate doping and large series resistance, only the low-frequency C-V characteristics at 2–20 kHz are shown here. Gate leakage characteristics of the three MOSCAPs are shown in (d).

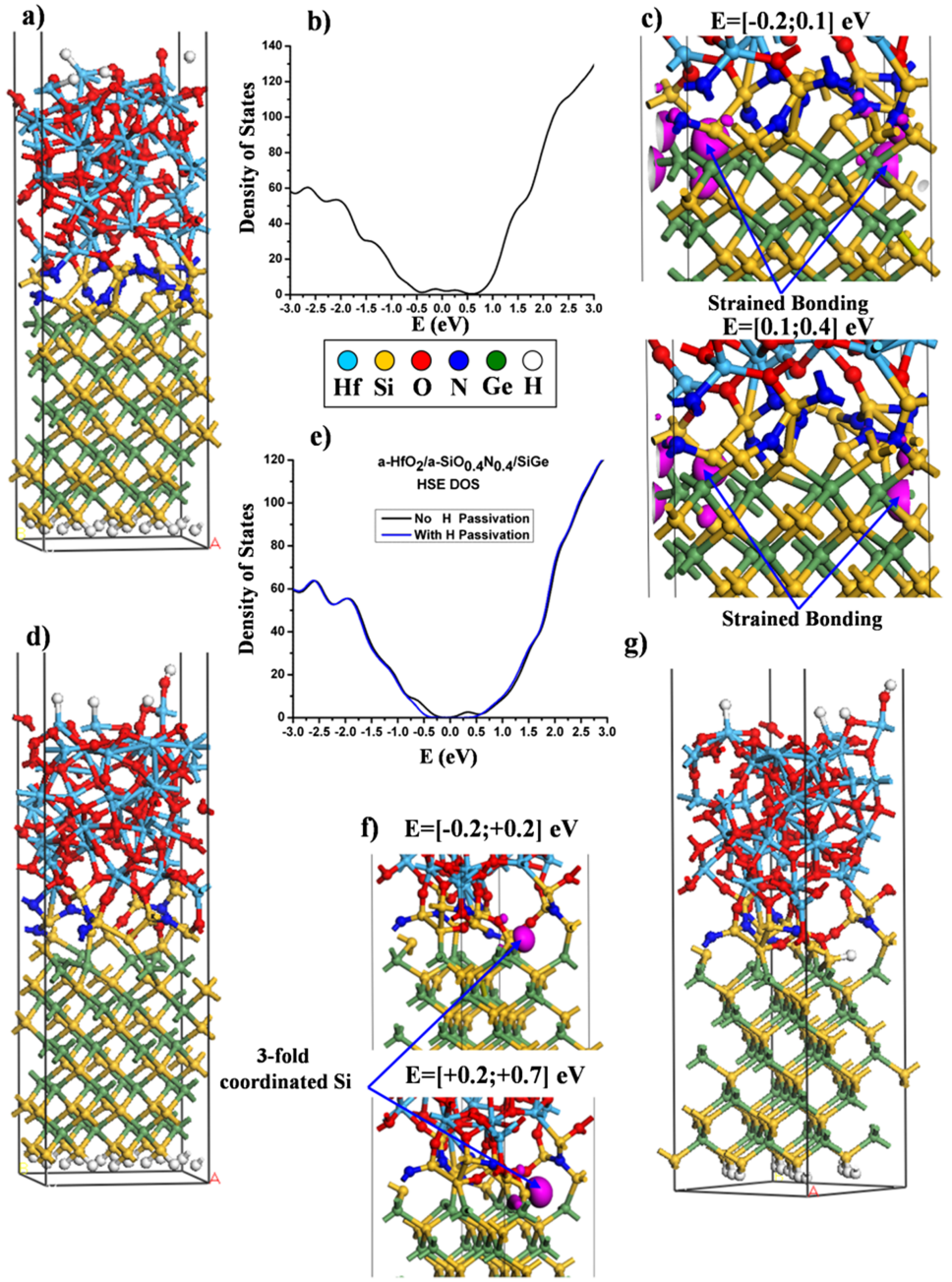

FIG. 9. DFT-MD simulations of gate stack a-HfO_2/a-SiO_xN_y/$Si_{0.5}Ge_{0.5}$(001). (a) a-HfO_2/a-Si_3N_2/SiGe stack with silicon-rich substoichiometric a-Si_3N_2 interfacial layer. (b) HSE06-calculated density of states of the gate stack shown in (a). E_F = 0.0 eV. (c) Band-decomposed charge density of a-HfO_2/a-Si_3N_2/SiGe with Si-rich substoichiometric a-Si_3N_2 interlayer at [−0.2; +0.1] eV and [+0.1, +0.4] eV. Pink lobes surround Si and Ge atoms with strained bonding found close to a-Si_3N_2/SiGe interface as pointed out by the blue arrows. (d) a-HfO_2/a-$SiO_{0.4}N_{0.4}$/SiGe stack with Si-rich substoichiometric a-$SiO_{0.4}N_{0.4}$ interfacial layer. (e) HSE06-calculated density of states of a-HfO_2/a-$SiO_{0.4}N_{0.4}$/SiGe stack without (d) and with H passivation (g). E_F = 0.0 eV for H-passivated (blue) curve. (f) a-HfO_2/a-$SiO_{0.4}N_{0.4}$/SiGe band-decomposed charge density visualized for the energy ranges of [−0.2; +0.2] and [+0.2; +0.7] eV showing a 3-fold under-coordinated Si atom at the a-$SiO_{0.4}N_{0.4}$/SiGe interface. (g) Gate stack shown in (d) with the 3-fold coordinated defective silicon atom passivated by a hydrogen atom.

DFT molecular dynamics (MD) simulations of a-HfO_2 on a-SiN_x and a-SiO_xN_y passivated $Si_{0.5}Ge_{0.5}$(001) surfaces are shown in Fig. 9. Fig. 9(a) shows the gate stack of a-HfO_2 on top of an interfacial layer of substoichiometric a-Si_3N_2 passivating the $Si_{0.5}Ge_{0.5}$(001) surface. The calculated HSE06 density of states for the gate stack is shown in Fig. 9(b), where defect states exist across the entire bandgap, and Fig. 9(c) shows the band-decomposed charged density for defect states in the energy ranges of [−0.2; +0.1] (eV), and [+0.1; +0.4] (eV) near the VB and CB. The defect states are indicated by pink lobes; the defect states are not in the interlayer but instead surround substrate Si and Ge atoms with strained bonding close to the a-Si_3N_2/SiGe interface (blue arrows).

Fig. 9(d) shows the gate stack of a-HfO_2 on top of a substoichiometric Si-rich a-$SiO_{0.4}N_{0.4}$ passivating interfacial layer on the $Si_{0.5}Ge_{0.5}$(001) surface. The calculated HSE06 density of states (Fig. 9(e)) shows the bandgap decreased by band-edge states and the Fermi level shifted to valence band. To identify sources of these band-edge states, the band-decomposed charge density was visualized for the energy ranges of [−0.2, +0.2] (near the VB) and [+0.2, +0.7] eV (near the CB) highlighting a 3-fold under-coordinated Si atom found below the a-SiON interfacial layer as a primary source of these band-edge states (Fig. 9(f)). Dangling bonds on gate-stacks have been passivated experimentally during forming gas annealing in a H_2/N_2 gas mixture. To simulate this process, a hydrogen atom was inserted and relaxed to passivate the under-coordinated silicon atom, as shown in Fig. 9(g). The calculated density of states curve (Fig. 9(e), blue curve with H passivation) shows that hydrogen passivation of the under-coordinated silicon

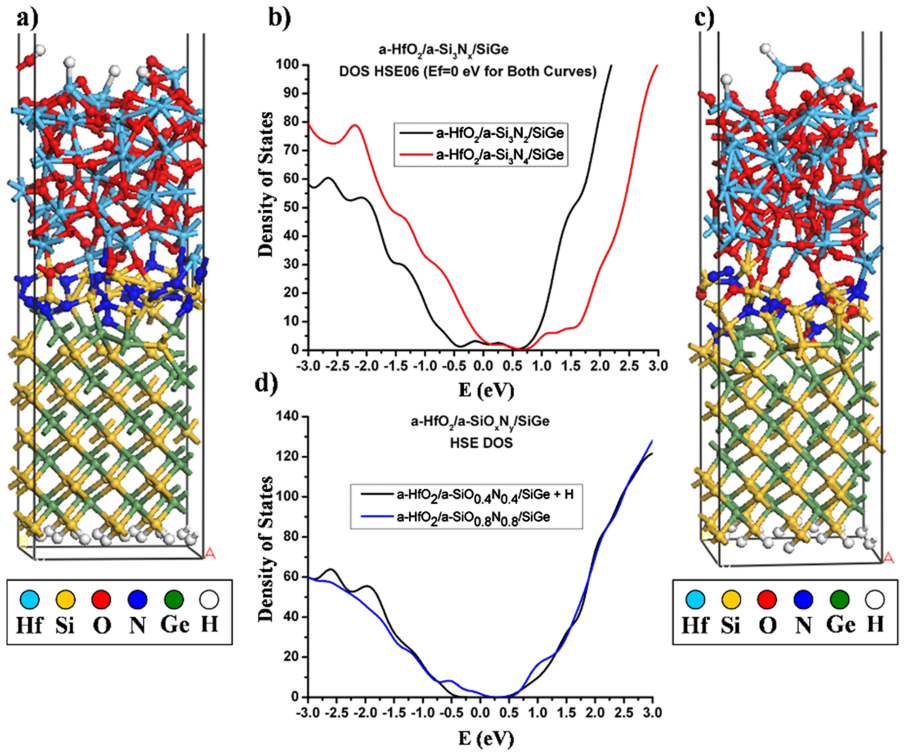

FIG. 10. DFT simulations of gate stack a-HfO_2/a-SiO_xN_y/$Si_{0.5}Ge_{0.5}$(001). (a) a-HfO_2/a-Si_3N_4/SiGe gate stack with stoichiometric a-Si_3N_4 interfacial layer. (b) Calculated density of states for a-HfO_2/a-Si_3N_4/SiGe stack (red curve) shown in (a) overlaid with results for a-HfO_2/a-Si_3N_2/SiGe (black curve) shown in Fig. 9(a). E_F = 0.0 eV for both curves. (c) a-HfO_2/a-$SiO_{0.8}N_{0.8}$/SiGe gate stack with stoichiometric a-$SiO_{0.8}N_{0.8}$ interfacial layer. (d) Calculated density of states for a-HfO_2/a-$SiO_{0.8}N_{0.8}$/SiGe stack (black curve) shown in (c) overlaid with the results for a-HfO_2/a-$SiO_{0.4}N_{0.4}$/SiGe stack (blue curve) shown in Fig. 9(g). E_F = 0.0 eV for black curve.

atom unpins the Fermi level by shifting the Fermi level into the band gap and expanding the band gap consistent with the experimental STS results for the substoichiometric passivating SiO_xN_y layer on the $Si_{0.7}Ge_{0.3}$(100) and $Si_{0.5}Ge_{0.5}$(100) surfaces.

Fig. 10(a) shows the DFT simulation of a-HfO_2 on top of an interfacial layer of stoichiometric a-Si_3N_4 passivating the $Si_{0.5}Ge_{0.5}$(001) surface. There is formation of Ge–N bonds, overcoordinated Si atoms, and strained bond angles in the SiGe substrate; note that the SiGe distortion is greater for the a-HfO_2/a-Si_3N_4/SiGe stack (Fig. 10(a)) than the a-HfO_2/a-Si_3N_2/SiGe stack (Fig. 9(a)). Fig. 10(b) shows the corresponding calculated density of states for the stack with the stoichiometric a-Si_3N_4 interlayer (Fig. 10(a)) with an overlay of the DOS from the stack with the substoichiometric a-Si_3N_2 interfacial layer (Fig. 9(a)). The calculated density of states for both gate stacks contains defect states throughout the band gap with Fermi level pinning. The results are consistent with a purely nitrided interlayer distorting the SiGe substrate creating band edge or band gap states.

Fig. 10(c) shows the DFT simulation of a-HfO_2 on top of an interfacial bilayer of stoichiometric a-$SiO_{0.8}N_{0.8}$ passivating the $Si_{0.5}Ge_{0.5}$(001) surface. Note that the a-HfO_2/a-$SiO_{0.8}N_{0.8}$/SiGe oxide stack induced formation of Ge–N bonds and distortion in the SiGe substrate are in contrast to the HfO_2/a-$SiO_{0.4}N_{0.4}$/SiGe oxide stack shown in Fig. 9(d). The HSE06 calculated density of states for a stoichiometric a-$SiO_{0.8}N_{0.8}$ layer (Fig. 10(c)) and a substoichiometric a-$SiO_{0.4}N_{0.4}$ interfacial layer (Fig. 9(d)) gate stacks are shown overlayed in Fig. 10(d). When comparing the gate stacks with the silicon rich substoichiometric a-$SiO_{0.4}N_{0.4}$ interlayer and stoichiometric a-$SiO_{0.8}N_{0.8}$ interlayer, the a-HfO_2/a-$SiO_{0.8}N_{0.8}$/SiGe stack has a small band gap and a Fermi level pinning in the valence band while the a-HfO_2/a-$SiO_{0.4}N_{0.4}$/SiGe oxide stack has a full band gap and an unpinned Fermi level consistent with the distortion of the SiGe by the a-HfO_2/a-$SiO_{0.8}N_{0.8}$ induced band edge state formation. In simple terms, when the interlayer is Si rich, O and N bonding to the substrate is minimized so this reduces breaking of bonds and bond angle strain in the SiGe substrate.

IV. CONCLUSIONS

ALD of a silicon rich SiN_x control layer on $Si_{0.7}Ge_{0.3}$(001), $Si_{0.5}Ge_{0.5}$(001), and $Si_{0.5}Ge_{0.5}$(110) surfaces has been achieved by sequential pulsing of Si_2Cl_6 and N_2H_4 precursors at a substrate temperature of 285 °C as shown by XPS. XPS measurements on SiGe(001) and SiGe(110) surfaces indicate that the SiO_xN_y thin film creates a diffusion barrier preventing Ge out diffusion as the germanium signal is largely attenuated following SiN_x ALD cycles, with Ge–N bonds localized to the SiO_xN_y/SiGe interface. STS measurements and DFT simulations confirm that the silicon rich SiO_xN_y interfacial control layer forms a passivating interfacial layer on the SiGe(001) surface, as the surface Fermi level was unpinned and the electronic structure was free of midgap trap states. DFT calculations show that a Si rich a-$SiO_{0.4}N_{0.4}$ film produces a lower interfacial defect density than stoichiometric a-$SiO_{0.8}N_{0.8}$, substoichiometric a-Si_3N_2, or stoichiometric a-Si_3N_4 interlayers because the Si rich a-$SiO_{0.4}N_{0.4}$ film minimizes bonding between the O and N atoms and the SiGe substrate thereby reducing strain and bond breaking in the SiGe by the interlayer. MOSCAP device fabrication on p-type $Si_{0.7}Ge_{0.3}$(001) and $Si_{0.5}Ge_{0.5}$(001) substrates with the insertion of an SiO_xN_y interfacial control layer shows a decrease in frequency dispersion and midgap trap states for a comparable C_{max} value.

SUPPLEMENTARY MATERIAL

See supplementary material for further DFT simulation details on generation of a-SiO_xN_y/SiGe interlayers, validation of a-HfO_2/a-SiO_xN_x/SiGe DFT-MD simulations, and experimental XPS raw peak analysis.

ACKNOWLEDGMENTS

The authors would like to acknowledge Applied Materials, Inc., as funding sources.

[1] S. Datta, J. Brask, G. Dewey, M. Doczy, B. Doyle, B. Jin, J. Kavalieros, M. Metz, A. Majumdar, and M. Radosavljevic, in *Bipolar/BiCMOS Circuits and Technology, Proceedings of the 2004 Meeting* (IEEE, 2004), p. 194.
[2] K. Rim, J. Welser, J. Hoyt, and J. Gibbons in *International Electron Devices Meeting (IEDM'95)* (IEEE, 1995), p. 517.
[3] J. Welser, J. Hoyt, and J. Gibbons in *International Electron Devices Meeting (IEDM'92), Technical Digest* (IEEE, 1992), p. 1000.
[4] K. J. Kuhn, IEEE Trans. Electron Devices **59**, 1813 (2012).
[5] J. Robertson and R. M. Wallace, Mater. Sci. Eng. R: Rep. **88**, 1 (2015).
[6] P. Bhatt, K. Chaudhuri, S. Kothari, A. Nainani, and S. Lodha, Appl. Phys. Lett. **103**, 172107 (2013).
[7] Y. Oshima, M. Shandalov, Y. Sun, P. Pianetta, and P. C. McIntyre, Appl. Phys. Lett. **94**, 183102 (2009).
[8] Y. Oshima, Y. Sun, D. Kuzum, T. Sugawara, K. C. Saraswat, P. Pianetta, and P. C. McIntyre, J. Electrochem. Soc. **155**, G304 (2008).
[9] R. Zhang, T. wasaki, N. Taoka, M. Takenaka, and S. Takagi, J. Electrochem. Soc. **158**, G178 (2011).
[10] K. Sardashti, K.-T. Hu, K. Tang, S. Madisetti, P. McIntyre, S. Oktyabrsky, S. Siddiqui, B. Sahu, N. Yoshida, and J. Kachian, Appl. Phys. Lett. **108**, 011604 (2016).
[11] J. Han, R. Zhang, T. Osada, M. Hata, M. Takenaka, and S. Takagi, Appl. Phys. Express **6**, 051302 (2013).
[12] W.-C. Yeh, R. Ishihara, S. Morishita, and M. Matsumura, Jpn. J. Appl. Phys., Part 1 **35**, 1509 (1996).
[13] R. A. Ovanesyan, D. M. Hausmann, and S. Agarwal, ACS Appl. Mater. Interfaces **7**, 10806 (2015).
[14] J. Klaus, A. Ott, A. Dillon, and S. George, Surf. Sci. **418**, L14 (1998).
[15] W.-J. Lee, J.-H. Lee, C.-O. Park, Y.-S. Lee, S.-J. Shin, and S.-K. Rha, Journal of the Korean Physical Society, **45**(5) 1352–1355 (2004).
[16] A. Nakajima, Q. D. Khosru, T. Yoshimoto, T. Kidera, and S. Yokoyama, Appl. Phys. Lett. **80**, 1252 (2002).
[17] S. Riedel, J. Sundqvist, and T. Gumprecht, Thin Solid Films **577**, 114 (2015).
[18] R. Xie, T. H. Phung, M. Yu, and C. Zhu, IEEE Trans. Electron Devices **57**, 1399 (2010).
[19] S. Zhu and A. Nakajima, Jpn. J. Appl. Phys., Part 1 **46**, 7699 (2007).
[20] H. Goto, K. Shibahara, and S. Yokoyama, Appl. Phys. Lett. **68**, 3257 (1996).
[21] W. Jang, H. Jeon, C. Kang, H. Song, J. Park, H. Kim, H. Seo, M. Leskela, and H. Jeon, Phys. Status Solidi A **211**, 2166 (2014).
[22] S. W. King, J. Vac. Sci. Technol. A **29**, 041501 (2011).
[23] S. Yokoyama, N. Ikeda, K. Kajikawa, and Y. Nakashima, Appl. Surf. Sci. **130**, 352 (1998).
[24] T. Ma, IEEE Trans. Electron Devices **45**, 680 (1998).
[25] S. Morishita, S. Sugahara, and M. Matsumura, Appl. Surf. Sci. **112**, 198 (1997).
[26] K. Park, W.-D. Yun, B.-J. Choi, H.-D. Kim, W.-J. Lee, S.-K. Rha, and C. O. Park, Thin Solid Films **517**, 3975 (2009).
[27] P. Mårtensson and R. Feenstra, Phys. Rev. B **39**, 7744 (1989).
[28] R. M. Feenstra, Surf. Sci. **299**, 965 (1994).
[29] R. M. Feenstra, J. A. Stroscio, and A. Fein, Surf. Sci. **181**, 295 (1987).
[30] R. M. Feenstra, J. Lee, M. H. Kang, G. Meyer, and K. H. Rieder, Phys. Rev. B **73**, 035310 (2006).
[31] R. M. Feenstra, Phys. Rev. B **50**, 4561 (1994).
[32] P. R. Bevington and D. K. Robinson, *Data Reduction and Error Analysis for the Physical Sciences*, 3rd ed. (McGraw-Hill, Boston, 2003).
[33] H.-P. Chen, Y. Yuan, B. Yu, J. Ahn, P. C. McIntyre, P. M. Asbeck, M. J. Rodwell, and Y. Taur, IEEE Trans. Electron Devices **59**, 2383 (2012).
[34] Y. Yuan, B. Yu, J. Ahn, P. C. McIntyre, P. M. Asbeck, M. J. Rodwell, and Y. Taur, IEEE Trans. Electron Devices **59**, 2100 (2012).
[35] G. Kresse and J. Furthmüller, Comput. Mater. Sci. **6**, 15 (1996).
[36] J. P. Perdew, K. Burke, and M. Ernzerhof, Phys. Rev. Lett. **77**, 3865 (1996).
[37] J. P. Perdew, K. Burke, and Y. Wang, Phys. Rev. B **54**, 16533 (1996).
[38] J. P. Perdew, K. Burke, and Y. Wang, Phys. Rev. B **57**, 14999 (1998).
[39] J. Heyd, G. E. Scuseria, and M. Ernzerhof, J. Chem. Phys. **118**, 8207 (2003).
[40] J. Heyd and G. E. Scuseria, J. Chem. Phys. **121**, 1187 (2004).
[41] J. Heyd, G. E. Scuseria, and M. Ernzerhof, J. Chem. Phys. **124**, 219906 (2006).
[42] A. V. Krukau, O. A. Vydrov, A. F. Izmaylov, and G. E. Scuseria, J. Chem. Phys. **125**, 224106 (2006).
[43] G. Kresse and D. Joubert, Phys. Rev. B **59**, 1758 (1999).
[44] P. E. Blöchl, Phys. Rev. B **50**, 17953 (1994).
[45] W. Press, B. Flannery, S. Teukolsky, and W. Vetterling, *Numerical recepies in C* (Cambridge University Press, New York, 1986).
[46] H. Stöhr and W. Klemm, Z. Anorg. Allg. Chem. **241**, 305–323 (1939).
[47] E. A. Chagarov and A. C. Kummel, J. Chem. Phys. **135**, 244705 (2011).
[48] E. A. Chagarov and A. C. Kummel, Surf. Sci. **602**, L74 (2008).
[49] E. Chagarov, L. Porter, and A. Kummel, J. Chem. Phys. **144**, 084704 (2016).
[50] E. Chagarov, K. Sardashti, T. Kaufman-Osborn, S. Madisetti, S. Oktyabrsky, B. Sahu, and A. Kummel, ACS Appl. Mater. Interfaces **7**, 26275 (2015).
[51] S. W. Park, T. Kaufman-Osborn, H. Kim, S. Siddiqui, B. Sahu, N. Yoshida, A. Brandt, and A. C. Kummel, J. Vac. Sci. Technol. A **33**, 041403 (2015).
[52] D.-S. Lin, S.-Y. Pan, and M.-W. Wu, Phys. Rev. B **64**, 233302 (2001).
[53] M. L. Huggins, J. Am. Chem. Soc. **75**, 4123 (1953).
[54] D. Aubel, M. Diani, J. Bischoff, D. Bolmont, and L. Kubler, J. Vac. Sci. Technol. B **12**, 2699 (1994).
[55] J. G. Speight, *Lange's Handbook of Chemistry* (McGraw-Hill, New York, 2005), Vol. 1.
[56] S. Tanuma, C. J. Powell, and D. R. Penn, Surf. Interface Anal. **21**, 165 (1994).
[57] G. Ingo, N. Zacchetti, D. Della Sala, and C. Coluzza, J. Vac. Sci. Technol. A **7**, 3048 (1989).
[58] F. Bell and L. Ley, Phys. Rev. B **37**, 8383 (1988).
[59] S. W. Park, H. Kim, E. Chagarov, S. Siddiqui, B. Sahu, N. Yoshida, J. Kachian, R. Feenstra, and A. C. Kummel, Surf. Sci. **652**, 322 (2016).
[60] H. Kondo, K. Kawaai, A. Sakai, M. Hori, S. Zaima, and Y. Yasuda, Jpn. J. Appl. Phys., Part 1 **46**, 71 (2007).
[61] C.-L. Wu, J.-L. Hsieh, H.-D. Hsueh, and S. Gwo, Phys. Rev. B **65**, 045309 (2002).